THE JOURNAL OF BIOLOGICAL CHEMISTRY VOL. 291, NO. 9, pp. 4407–4416, February 26, 2016

Fast or Slow, Either Head Can Start the Processive Run of Kinesin-2 KIF3AC*

Received for publication, November 21, 2015, and in revised form, December 16, 2015 Published, JBC Papers in Press, December 28, 2015, DOI 10.1074/jbc.M115.705970

Pengwei Zhang[‡], **Ivan Rayment**[§], **and Susan P. Gilbert**[‡1]

From the [‡]*Department of Biological Sciences and the Center for Biotechnology and Interdisciplinary Studies, Rensselaer Polytechnic Institute, Troy, New York 12180 and the* [§]*Department of Biochemistry, University of Wisconsin, Madison, Wisconsin 53706*

Mammalian KIF3AC contains two distinct motor polypeptides and is best known for its role in organelle transport in neurons. Our recent studies showed that KIF3AC is as processive as conventional kinesin-1, suggesting that their ATPase mechanochemistry may be similar. However, the presence of two different motor polypeptides in KIF3AC implies that there must be a cellular advantage for the KIF3AC heterodimer. The hypothesis tested was whether there is an intrinsic bias within KIF3AC such that either KIF3A or KIF3C initiates the processive run. To pursue these experiments, a mechanistic approach was used to compare the pre-steady-state kinetics of KIF3AC to the kinetics of homodimeric KIF3AA and KIF3CC. The results indicate that microtubule collision at 11.4 μM^{-1} s^{-1} coupled with ADP release at 78 s^{-1} are fast steps for homodimeric KIF3AA. In contrast, KIF3CC exhibits much slower microtubule association at 2.1 μM^{-1} s^{-1} and ADP release at 8 s^{-1}. For KIF3AC, microtubule association at 6.6 μM^{-1} s^{-1} and ADP release at 51 s^{-1} are intermediate between the constants for KIF3AA and KIF3CC. These results indicate that either KIF3A or KIF3C can initiate the processive run. Surprisingly, the kinetics of the initial event of microtubule collision followed by ADP release for KIF3AC is not equivalent to 1:1 mixtures of KIF3AA plus KIF3CC homodimers at the same motor concentration. These results reveal that the intermolecular communication within the KIF3AC heterodimer modulates entry into the processive run regardless of whether the run is initiated by the KIF3A or KIF3C motor domain.

Kinesin-2 subfamily members are best known for their roles in long distance cargo transport, but unlike other processive kinesins, the kinesin-2 subfamily includes both homodimeric and heterodimeric kinesins (reviewed in Refs. 1–3). In mammals, there are four kinesin-2 subfamily genes: *KIF3A*, *KIF3B*, *KIF3C*, and *KIF17* (4–17). When expressed, KIF17 forms homodimers, yet KIF3A associates with either KIF3B or KIF3C to form the heterodimers KIF3AB and KIF3AC. In each case, these kinesin-2 molecular motors associate with nonmotor adaptor proteins to link the kinesin to its specific cargo (6, 15, 18–27). Of the kinesin-2 adaptors, the kinesin-associated protein KAP with KIF3AB has resulted in the designation of KIF3AB-KAP as a heterotrimeric kinesin (6, 18–22, 26). KIF3AB and KIF17 have been widely studied in multiple model organisms including *Caenorhabditis elegans*, *Drosophila melanogaster*, *Danio rerio*, as well as *Mus musculus* to understand their roles in intraflagellar transport and organelle transport for many other cellular functions (1–3). In contrast, KIF3AC has not been as well studied because there is not a true *KIF3C* ortholog in many of these model organisms. KIF3C exhibits a signature motif conserved in mammalian species, a 25-residue insert in loop L11 of the catalytic motor domain, which is enriched in glycines and serines (7, 28–30). This L11 insert is not present in other kinesins. Furthermore, even though KIF3AB and KIF3AC share similarities in protein sequence and structure, KIF3AC appears to function specifically in neurons rather than ubiquitously as do KIF3AB and KIF17 (1, 2, 28).

Recent single molecule studies revealed that heterodimers of KIF3AC and KIF3AB were as processive as kinesin-1 K560 based on their run lengths, indicating that KIF3AC and KIF3AB have the capacity for long distance intracellular transport (30). Furthermore, to begin to tease apart the contributions of each motor head, homodimers of KIF3AA, KIF3BB, and KIF3CC were generated and characterized. The results for KIF3AA in comparison with KIF3CC were striking because despite sequence similarity between KIF3A and KIF3C, KIF3AA was a very fast and processive kinesin, yet KIF3CC, although processive, was exceedingly slow (Table 1). In contrast, the properties of KIF3AA and KIF3BB were more similar to each other (30, 31). This obvious disparity between KIF3AA and KIF3CC raises the question of what is the contribution of each motor head for KIF3AC function.

To address this question, a pre-steady-state ATPase kinetics analysis was pursued for KIF3AC in comparison with KIF3AA and KIF3CC. The experiments asked specifically whether there was an intrinsic bias within KIF3AC such that either KIF3A or KIF3C initiated the processive run and whether heterodimerization alters the intrinsic properties of KIF3A and KIF3C by intermolecular communication.

Experimental Procedures

Constructs of Homodimeric and Heterodimeric KIF3—The *M. musculus KIF3A* and *KIF3C* plasmids for expression of KIF3AC heterodimers and the KIF3AA and KIF3CC homodimers were described previously in detail (30). The construct

* This work was supported, in whole or in part, by National Institutes of Health Grants R37-GM054141 (to S. P. G.) and R01-GM086351 (to I. R.). The authors declare that they have no conflicts of interest with the contents of this article. The content is solely the responsibility of the authors and does not necessarily represent the official views of the National Institutes of Health.
[1] To whom correspondence should be addressed: Dept. of Biological Sciences and the Center for Biotechnology and Interdisciplinary Studies, Rensselaer Polytechnic Inst., Troy, NY 12180. Tel.: 518-276-4415; E-mail: sgilbert@rpi.edu.

for *KIF3A* when expressed as a heterodimer with *KIF3C* includes the native sequence of the motor domain, the neck linker, and helix α7 (Met^1–Leu^{374}), followed by the dimerization motif of EB1 (DFYFGKLRNIELICQENEGENDPVLQRIVDILYATDE) and the C-terminal tobacco etch virus protease-cleavable Strep tag (TTSENLYFQGASNWSHPQFEK). The *KIF3C* construct for KIF3AC includes the native sequence of the KIF3C motor domain, neck linker, and helix α7 (Met^1–Leu^{374}), followed by the dimerization motif of EB1 (DFYFGKLRNIELICQENEGENDPVLQRIVDILYATDE) and the tobacco etch virus protease-cleavable His_8 tag (TTSENLYFQGASHHHHHHHH). The KIF3AA homodimer contained the same sequence as the construct for the heterodimer, except the purification tag used was the His_8 tag. The plasmid for KIF3CC homodimer expression is the same as for heterodimer expression. The resulting constructs were sequence-verified over the entire ORF insert (30).

KIF3 Protein Expression and Purification—KIF3 motors were expressed in *Escherichia coli* BL21-CodonPlus (DE3)-RIL cell line (Stratagene, La Jolla, CA) for purification as described in detail previously (30, 32). To achieve the purification of KIF3AC heterodimers, sequential affinity columns were used. The HisTrap FF Ni^{+2}-NTA column (GE Healthcare) selected for KIF3C because of its C-terminal His_8 tag, and the StrepTactin™ column (GE Healthcare) selected for the Strep-tagged KIF3A. The purified KIF3AC was evaluated by analytical gel filtration chromatography (Superose™ 10/300; GE Healthcare) and SDS-PAGE to confirm purification of stable heterodimers with a 1:1 stoichiometry of KIF3A to KIF3C. The predicted molecular weight based on amino acid sequence of KIF3AC is 98,317.

To purify homodimeric KIF3AA or KIF3CC, the supernatant of the cell lysate was loaded onto the HisTrap FF Ni^{+2}-NTA column (GE Healthcare) to select for the specific homodimer expressed. The purified homodimers of KIF3AA or KIF3CC were analyzed by analytical gel filtration and SDS-PAGE. The predicted molecular weights based on amino acid sequence of KIF3AA and KIF3CC are 97,000 and 99,518, respectively.

The KIF3 proteins were dialyzed against ATPase buffer containing 20 mM Hepes, pH 7.2, with KOH, 5 mM magnesium acetate, 0.1 mM EDTA, 0.1 mM EGTA, 50 mM potassium acetate, 1 mM dithiothreitol, plus 5% sucrose followed by ultracentrifugation to remove aggregates and then frozen as aliquots in liquid N_2 for storage at −80 °C. Before each experiment, KIF3 protein aliquots were thawed and clarified for 10 min at 4 °C (Beckman Coulter TLX Optima Ultracentrifuge, TLA-100 rotor, 313,000 × *g*), and the protein concentration was determined using the Bio-Rad protein assay with IgG as a protein standard. The experiment is designed using the KIF3 dimer concentration but converted to the ATP site concentration (two sites per dimer) to report here.

Experimental Conditions—The experiments were performed at 25 °C in ATPase buffer: 20 mM Hepes, pH 7.2, with KOH, 5 mM magnesium acetate, 0.1 mM EDTA, 0.1 mM EGTA, 50 mM potassium acetate, 1 mM dithiothreitol, plus 5% sucrose. The morning of each experiment bovine tubulin was cold-depolymerized, clarified, and polymerized with 1 mM MgGTP at

$$MT + E{\bullet}ADP \overset{1}{\rightleftharpoons} MT{\bullet}E{\bullet}ADP \overset{2}{\rightleftharpoons} MT{\bullet}E + ADP$$

$$MT{\bullet}E + ATP \overset{3}{\rightleftharpoons} MT{\bullet}E{\bullet}ATP \overset{3'}{\rightleftharpoons} MT{\bullet}E^*{\bullet}ATP \overset{4}{\rightleftharpoons} MT{\bullet}E{\bullet}ADP{\bullet}P_i \overset{5}{\rightleftharpoons} MT + E{\bullet}ADP + P_i$$

SCHEME 1

37 °C, followed by MT[2] stabilization with 40 μM paclitaxel. The MT concentrations reported represent those of the paclitaxel-stabilized tubulin polymer. The reported concentrations of ATP, GTP, and the nucleotide analog mantATP include an equivalent concentration of magnesium acetate. Note that the fluorescent analog mantATP was purchased from Invitrogen as the isomeric mixture. The errors are reported as S.E.

MantATP Binding Kinetics—To determine the second order rate constant of ATP binding, the fluorescent ATP analog, mantATP (Invitrogen), was used. The MT·KIF3 complexes were preformed and rapidly mixed with mantATP in the stopped-flow instrument (KinTek SF2003; KinTek Corp., Austin, TX). The change in the relative fluorescence of mantATP was monitored by excitation at 360 nm with detection at ~450 nm using a 409-nm long pass filter (Semrock Inc.). Upon mantATP binding to the hydrophobic pocket of the active site, the fluorescence was enhanced, and a double exponential function was fit to each biphasic transient (see Fig. 1). The observed rates of the initial fast exponential phase of each transient were plotted as a function of increasing mantATP concentration. The following equation was fit to the data,

$$k_{obs} = k_{+1}[\text{MantATP}] + k_{-1} \quad \text{(Eq. 1)}$$

where k_{obs} is the observed rate of the initial exponential phase, k_{+1} represents the second order rate constant for mantATP binding, and k_{-1} is the dissociation rate constant obtained from the *y* intercept. The observed rates of the second exponential phase of each transient were also plotted as a function of mantATP concentration, and a hyperbolic function was fit to these data (see Fig. 1, Scheme 1, and Table 1).

Pulse-Chase Kinetics of ATP Binding—To determine the time course of ATP binding, a chemical quench-flow instrument (RQF-3, KinTek Corp.) was used (32, 33). The MT·KIF3AC complex (5 μM KIF3AC/40 μM MTs or 10 μM KIF3AC/40 μM MTs, syringe concentrations) was rapidly mixed with MgATP plus radiolabeled [α-^{32}P]ATP and 300 mM KCl (syringe concentrations) for times ranging from 5 to 200 ms in the instrument. The reaction was subsequently chased with 30 mM nonradiolabeled MgATP plus 150 mM KCl (syringe concentrations) for 0.7 s (>10 ATP turnovers) and then expelled from the instrument into an Eppendorf tube containing 100 μl of 22 N formic acid. The acid terminates the reaction, unfolds the protein, and releases nucleotide from the active site. During the time of chase, stably bound [α-^{32}P]ATP was converted to [α-^{32}P]ADP·P_i, whereas any [α-^{32}P]ATP unbound or bound loosely to the active site was diluted by the high concentration of nonradiolabeled ATP. The nucleotide products ([α-^{32}P]ADP + P_i) were separated from the substrate [α-^{32}P]ATP by thin layer chromatography and quantified by using Image Gauge V4 software (FUJIFILM Science Laboratory). The con-

[2] The abbreviations used are: MT, microtubule; mantATP, 2′-(or 3′)-*O*-(*N*-methylanthraniloyl)ATP.

centration of [α-^{32}P]ADP product was plotted as a function of time. Equation 2 was fit to each transient,

$$[\text{ADP}] = A_0[1 - \exp(-k_b t)] + k_{slow} t \quad \text{(Eq. 2)}$$

where A_0 is the amplitude of the exponential phase, representing the concentration of stably bound ATP that proceeded through ATP hydrolysis during the first ATP turnover, k_b is the observed rate of the exponential phase, and t is the time in seconds. The k_{slow} is the rate constant of the linear phase (μM·s^{-1}) and, when divided by the active site concentration, corresponds to steady-state turnover at the conditions of the experiment. The observed exponential rates of each transient were plotted as a function of MgATP concentration, and Equation 3 was fit to the data,

$$k_{obs} = [K_1 k_{+1}'[\text{ATP}]/(K_1[\text{ATP}] + 1)] \quad \text{(Eq. 3)}$$

where K_1 represents the equilibrium association constant for collision complex formation ($K_d = 1/K_1$), and k'_{+1} is the first order rate constant for the ATP-promoted isomerization. The amplitude of each transient was plotted as a function of increasing MgATP concentration, and the hyperbolic fit to the data provided the maximum amplitude of the exponential phase (see Fig. 2, *A–C*, Scheme 1, and Table 1).

Acid-quench Kinetics of ATP Hydrolysis—To measure the time course of ATP hydrolysis, the MT·KIF3AC complex (10 μM KIF3AC and 40 μM MTs, syringe concentrations) was rapidly mixed with MgATP plus trace [α-^{32}P]ATP and 300 mM KCl (syringe concentrations) for times ranging from 5 to 300 ms in a KinTek chemical quench-flow instrument (32, 33). The reaction was terminated with 22 N formic acid and expelled from the instrument. The products [α-^{32}P]ADP + P_i were separated from [α-^{32}P]ATP and quantified, and the concentration of [α-^{32}P]ADP was plotted as a function of time. Equation 2 was fit to each transient, yielding the observed rate and amplitude, which were plotted as a function of MgATP concentration. A hyperbolic function was fit to each data set, thereby providing the rate constant of ATP hydrolysis and the maximum amplitude of the initial exponential phase that corresponds to the first ATP turnover (see Fig. 2, *D–F*, Scheme 1, and Table 1).

ADP Release upon MT Collision—To measure the kinetics of ADP release upon MT collision, the experimental design mimicked the reaction condition at the beginning of the cycle (see Fig. 5, E0–E1). KIF3 motors were rapidly mixed in the stopped-flow instrument with MTs plus mantATP. At the conditions of the assay, mantATP binding was significantly faster than ADP release from the active site upon MT collision. Therefore, the enhanced fluorescence upon mantATP binding was used as a readout of ADP release. KIF3 at 0.5, 1, or 5 μM sites was rapidly mixed with 0.5–50 μM MTs plus 50 or 100 μM mantATP in the stopped-flow instrument. The final concentrations were 0.25 or 0.5 μM KIF3 sites and 25 μM mantATP for 0.25–2.25 μM MTs or 2.5 μM KIF3 sites and 50 μM mantATP for 2.5–25 μM MTs. A double exponential function was fit to each transient. The observed rates of the initial exponential phase were plotted as a function of MT concentration, and the hyperbolic fit to the data provided the maximum rate constant of ADP release. At low concentrations of MTs, the observed rate of ADP release is limited by MT collision; therefore, the linear fit to these data provided the second order rate constant of MT association (see Fig. 3, Scheme 1, and Table 1).

Is There an Intrinsic Bias of Which KIF3 Head Initiates the Processive Run?—To test this hypothesis, additional ADP release experiments were performed as described in the previous section. KIF3AC, KIF3AA, KIF3CC, and mixtures of KIF3AA + KIF3CC at 5 μM KIF3 site concentration were rapidly mixed with 30 μM MTs plus 100 μM mantATP (syringe concentrations). The final concentrations were 2.5 μM KIF3 site concentration, 15 μM MTs, and 50 μM mantATP. The mixtures corresponded to 75% KIF3AA + 25% KIF3CC, 50% KIF3AA + 50% KIF3CC, and 25% KIF3AA + 75% KIF3CC. A double exponential fit to each transient provided the rate constants and relative amplitudes of each exponential phase (see Fig. 4).

To further analyze the transients of the KIF3AA and KIF3CC mixtures of homodimers, equivalent transients were generated computationally. Each stopped-flow transient represents a thousand data points during the collection time, with each data point representing the relative fluorescence output for the KIF3 sites. Therefore, the experimental transients can be evaluated using the data from KIF3AA and KIF3CC transients to computationally generate a transient at the appropriate composition of the KIF3AA + KIF3CC experimental curve. For example, to generate a computationally derived transient for 50% KIF3AA + 50% KIF3CC, the data for the time courses of 100% KIF3AA and 100% KIF3CC were each divided by 2 and summed to generate a computationally derived transient. These computationally derived transients were then compared directly to the experimental transients for the mixtures and the transient for KIF3AC (see Fig. 4*B*).

Results

Scheme 1 is the KIF3AC ATPase pathway used to design the pre-steady-state kinetics experiments, and Fig. 5 presents a stepping model of the KIF3AC interactions with the MT. The rate and equilibrium constants are reported in Table 1.

MantATP Binding Kinetics—To determine the kinetics of ATP binding, two approaches were used. In the first, the fluorescence enhancement of the analog mantATP binding to the KIF3 motors was monitored (Fig. 1). For the second (Fig. 2, *A–C*), a pulse-chase approach with radiolabeled ATP was used. For the mantATP binding kinetics, the preformed MT·KIF3 complex was rapidly mixed in the stopped-flow instrument with increasing concentrations of mantATP. Fig. 1*A* shows representative transients of mantATP binding to the MT·KIF3AC complex, and the biphasic kinetics required a double exponential fit to each transient. The observed rates of the initial exponential phase were plotted as a function of increasing mantATP concentration (Fig. 1*B*), and the linear fit of the data provided the second order rate constant of mantATP binding at 11 μM^{-1} s^{-1}. The *inset* in Fig. 1*B* reveals that the second phase of mantATP binding was also mantATP concentration-dependent, and the hyperbolic fit to the data provided the rate of 22 s^{-1}. Because the steady-state k_{cat} for KIF3AC is 21.5 s^{-1}, these results are consistent with an alternating site model for KIF3AC as proposed in Fig. 5.

TABLE 1
KIF3AC, KIF3AA, and KIF3CC experimentally determined constants

	KIF3AC	KIF3AA	KIF3CC
Microtubule association	$k_{+1} = 6.6 \pm 0.2\ \mu M^{-1}\ s^{-1}$	$k_{+1} = 11.4 \pm 0.6\ \mu M^{-1}\ s^{-1}$	$k_{+1} = 2.1 \pm 0.1\ \mu M^{-1} s^{-1}$
	Not observed	$k_{-1} = 2.4 \pm 0.9\ s^{-1}$	$k_{-1} = 0.6 \pm 0.1\ s^{-1}$
ADP release	$k_{+2} = 51.4 \pm 2.2\ s^{-1}$	$k_{+2} = 77.7 \pm 1.4\ s^{-1}$	$k_{+2} = 7.6 \pm 0.1\ s^{-1}$
	$K_{1/2,MT} = 6.3 \pm 0.7\ \mu M$	$K_{1/2,MT} = 4.4 \pm 0.2\ \mu M$	$K_{1/2,MT} = 1.7 \pm 0.1\ \mu M$
MantATP binding	$k_{+3} = 11.0 \pm 0.6\ \mu M^{-1}\ s^{-1}$	$k_{+3} = 16.0 \pm 0.5\ \mu M^{-1}\ s^{-1}$	$k_{+3} = 0.68 \pm 0.04\ \mu M^{-1}\ s^{-1}$
	$k_{-3} = 21.4 \pm 7.2\ s^{-1}$	$k_{-3} = 10.5 \pm 5.1\ s^{-1}$	$k_{-3} = 7.7 \pm 0.4\ s^{-1}$
Pulse chase	$K_3 = 0.3 \pm 0.03\ \mu M^{-1}$	N.D.[a]	N.D.
	$k'_{+3} = 81.0 \pm 1.0\ s^{-1}$		
	$K_3 k'_{+3} = 24.3\ \mu M^{-1}\ s^{-1}$		
	$K_{d,ATP} = 3.3\ \mu M$		
	$A_{max} = 0.8 \pm 0.02$ per site		
	$K_{d,ATP} = 23.4 \pm 2.5\ \mu M$		
Acid quench	$k_{+4} = 69.1 \pm 1.2\ s^{-1}$	N.D.	N.D.
	$K_{d,ATP} = 9.7 \pm 0.9\ \mu M$		
	$A_{max} = 0.77 \pm 0.02$ per site		
	$K_{d,ATP} = 18.8 \pm 1.9\ \mu M$		
Steady-state parameters[b]	$k_{cat} = 21.5 \pm 0.3\ s^{-1}$	$k_{cat} = 34.7 \pm 0.5\ s^{-1}$	$k_{cat} = 1.1 \pm 0.02\ s^{-1}$
	$K_{m,ATP} = 138.1 \pm 12.8\ \mu M$	$K_{m,ATP} = 47.7 \pm 0.1\ \mu M$	$K_{m,ATP} = 4.8 \pm 0.5\ \mu M$
	$K_{1/2,MT} = 232.8 \pm 26.6$ nM	$K_{1/2,MT} = 192.9 \pm 1.7$ nM	$K_{1/2,MT} = 44.3 \pm 7.4$ nM
Velocity[b]	$V_{max} = 186.5 \pm 5.6$ nm/s	$V_{max} = 239.2 \pm 4.2$ nm/s	$V_{max} = 7.5 \pm 0.4$ nm/s
	K_m,ATP $= 84 \pm 0.1\ \mu M$	N.D.	N.D.
Run length[b]	$1.23 \pm 0.09\ \mu m$	$0.98 \pm 0.05\ \mu m$	$0.57 \pm 0.03\ \mu m$

[a] N.D., not determined.
[b] Steady-state ATPase parameters and single molecule velocity and run length data from Ref. 30.

The results in Fig. 1*C* show that mantATP also binds the MT·KIF3AA complex rapidly at 16 $\mu M^{-1}\ s^{-1}$. In contrast, KIF3CC displays a very slow second order rate constant for mantATP binding at 0.68 $\mu M^{-1}\ s^{-1}$. These results are consistent with our previous studies in which the steady-state ATPase kinetics and single molecule velocities for KIF3AA were faster than those for KIF3AC, and KIF3CC was a dramatically slower motor (Table 1 and Ref. 30). The mantATP results also reveal that at this early step in the pathway (Fig. 5, E1–E2), the KIF3A head is very different from the KIF3C head based on the results for homodimeric KIF3AA and KIF3CC.

ATP Binding and ATP Hydrolysis Are Both Fast Events for KIF3AC—The kinetics of ATP binding were also measured by the pulse-chase approach using radiolabeled ATP (Fig. 2, *A–C*). The MT·KIF3AC complex was preformed and rapidly mixed with [α-^{32}P]ATP in the chemical quench-flow instrument for times from 5 to 200 ms and subsequently chased with a high concentration of unlabeled MgATP for 0.7 s. During the time of the ATP chase, unbound [α-^{32}P]ATP and loosely bound [α-^{32}P]ATP were diluted by the high concentration of unlabeled ATP. However, [α-^{32}P]ATP stably bound to the active site proceeds through ATP hydrolysis. Therefore, this experimental design quantifies the MT·KIF3AC*·[α-^{32}P]ATP intermediate that proceeds through ATP hydrolysis (Scheme 1). Because of the high processivity of KIF3AC, an additional 300 mM KCl (syringe concentration) was added to the [α-^{32}P]ATP syringe, and 150 mM KCl was added to the ATP chase syringe. The additional salt does not affect the first turnover but slows steady-state ATP turnover and therefore enables the initial exponential burst phase to be better resolved.

Each transient displayed two phases: the initial exponential phase corresponding to the first ATP turnover and the following linear phase representing subsequent ATP binding events or steady-state activity (Fig. 2*A*). The observed rates of the initial exponential phase of each transient were plotted as a function of ATP concentration. Equation 3 was fit to the data, yielding the maximum rate constant at 81 s^{-1} with $K_{d,ATP}$ at 3.3 μM (Fig. 2*B*). This rate constant represents the rate of the ATP-promoted isomerization that occurs to generate the MT·KIF3*·ATP intermediate poised for ATP hydrolysis (Scheme 1 and Table 1).

The amplitude (A_0) of the exponential phase represents the concentration of [α-^{32}P]ATP bound at the active site that proceeded to form the product [α-^{32}P]ADP·P_i during the first ATP turnover. The observed amplitude from each transient was plotted as a function of increasing concentrations of ATP. The maximum amplitude at 0.8 μM ADP·P_i per μM active site concentration indicates that approximately one ATP turnover occurred before KIF3AC detachment from MT (Fig. 2*C*).

To determine the time course of ATP hydrolysis (Fig. 2, *D–F*), the acid-quench experiments were performed at the same concentrations of the MT·KIF3AC complex as in the pulse-chase experiments, and 300 mM KCl (syringe concentration) was also added to the [α-^{32}P]ATP syringe to slow steady-state ATP turnover to better define the first ATP turnover. The concentration of [α-^{32}P]ADP·P_i product formed was plotted as a function of time. Each transient was also biphasic with an initial exponential phase followed by a linear phase, indicative that a slow step occurred after ATP hydrolysis (Fig. 2*D*). The observed rates of the initial exponential phase were plotted as a function of increasing ATP concentration, and the hyperbolic fit to the data provided the maximum rate constant of ATP hydrolysis at 69 s^{-1} with the $K_{d,ATP}$ at 9.7 μM (Fig. 2*E* and Table 1). Fig. 2*F* presents the burst amplitude data (A_0) of the exponential phase plotted as a function of ATP concentration, and the hyperbolic fit to the data provided A_{max} of 0.77 μM ADP·P_i per μM KIF3AC active site concentration. The amplitude data for both the pulse-chase kinetics and the acid-quench kinetics are consistent with the interpretation that each motor head (KIF3A or KIF3C) were able to bind and hydrolyze one ATP during the first ATP turnover.

In sum, these results from the pulse-chase and acid-quench experiments show that ATP binding and ATP hydrolysis for KIF3AC are both fast events. Furthermore, the observation that

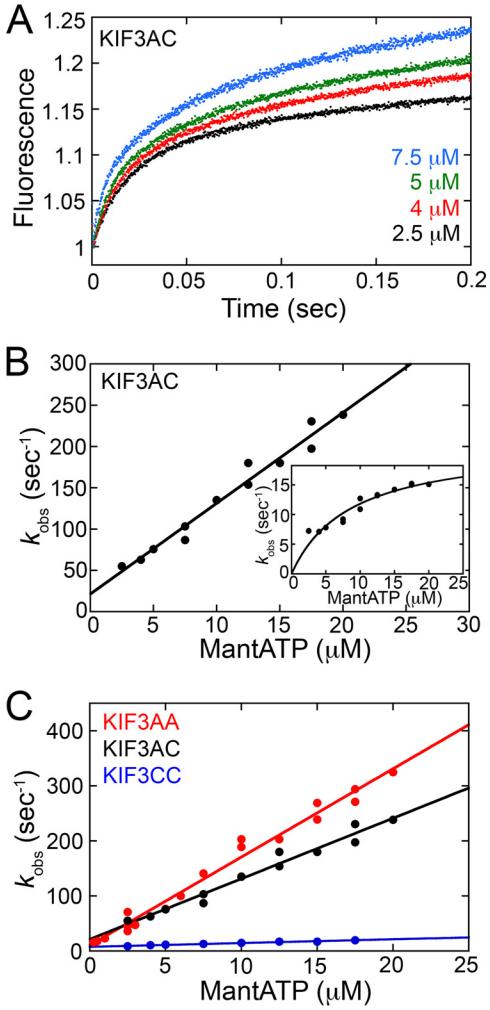

FIGURE 1. **MantATP binding.** The preformed MT·KIF3 complex was rapidly mixed in the stopped-flow instrument with increasing concentrations of mantATP. The final concentrations were 0.5 μM KIF3 sites or 2.5 μM KIF3 sites, 7.5 μM MTs, and 0.5–20 μM mantATP. *A*, representative transients of KIF3AC show an exponential increase in fluorescence as a function of time, and a double exponential function fit to each provided the observed rates of each phase. *B*, the observed rates of the initial exponential phase of KIF3AC were plotted as a function of mantATP concentration, and the linear fit (Equation 1) to the data provided the second order rate constant for mantATP binding at 11.0 ± 0.6 μM^{-1} s^{-1} with k_{off} = 21.4 ± 7.2 s^{-1}. The *inset* presents the observed rates of the second exponential phase, and the hyperbolic fit provides k_{max} at 22.0 ± 2.1 s^{-1} with $K_{1/2,mantATP}$ at 8.6 ± 1.9 μM. *C*, the observed rates of the initial exponential phase were plotted as a function of mantATP concentration, and the linear fit to the data provided the second order rate constant for mantATP binding for KIF3AA at 16.0 ± 0.5 μM^{-1} s^{-1} with k_{off} = 10.5 ± 5.1 s^{-1} and KIF3CC at 0.68 ± 0.04 μM^{-1} s^{-1} with k_{off} = 7.7 ± 0.4 s^{-1} in comparison with the data for KIF3AC also shown in *B*.

the maximum amplitude at ~0.8 indicates that the experimental design were able to separate the first ATP turnover from the subsequent ATP turnovers despite the high processivity of KIF3AC.

KIF3AC and KIF3AA Microtubule Collision Is Significantly Faster than Microtubule Collision by KIF3CC—To measure the kinetics of MT collision and ADP release, we designed an experiment to measure native ADP release rather than mantADP release. Because the binding of mantATP is so rapid (Fig. 1 and Table 1), we can use the fluorescence signal for mantATP binding as a readout of MT collision followed by ADP release. For this experiment, the KIF3 motors were rapidly mixed in the stopped-flow instrument with MTs plus mantATP (Fig. 3). At low MT concentrations, ADP release is limited by the collision of KIF3 with the MT; therefore, the linear fit of the data in this concentration range provides the second order rate constant for MT association. The rate constant of MT association by KIF3AC is 6.6 μM^{-1} s^{-1} (Fig. 3*B*) with KIF3AA at 11.4 μM^{-1} s^{-1} (Fig. 3*C*). In contrast, MT collision by KIF3CC is significantly slower at 2.1 μM^{-1} s^{-1} (Fig. 3*D*). Note that the MT association rate of KIF3AC is intermediate between the constants for KIF3AA and KIF3CC (Fig. 3*E*).

The ADP Release Kinetics of KIF3AC Are Intermediate between KIF3AA and KIF3CC—As the MT concentration in these experiments is increased, the data become hyperbolic and represent the rate of ADP release that directly follows MT collision. The rate constant for KIF3AA was 78 s^{-1}, whereas KIF3CC exhibits a much slower maximum rate of ADP release at 8 s^{-1} (Fig. 3, *C–E*). In contrast, the corresponding rate constant of ADP release for KIF3AC was observed at 51 s^{-1}, which is intermediate between the constants for KIF3AA and KIF3CC (Fig. 3*E*).

The MT association and ADP release kinetics can be interpreted as follows. If there were an intrinsic bias of entry into the processive run (Fig. 5, E0–E1), we would expect the kinetics of KIF3AC to be more similar to the kinetics of either KIF3AA or KIF3CC. In contrast, for both MT association and MT-promoted ADP release, the kinetics for both events for KIF3AC are intermediate between those for KIF3AA and KIF3CC, suggesting that either head, KIF3A or KIF3C, can begin the processive run. Note too that the transients for KIF3AC (Fig. 3*A*) are biphasic with the initial phase rapid followed by a slower phase at 4–8 s^{-1}, and the amplitude is approximately split between the two phases. In contrast to KIF3AC, the transients for KIF3AA and KIF3CC are not strictly biphasic with the amplitude associated with the first exponential phase followed by a slow linear phase (Fig. 4).

Intermolecular Communication Modulates KIF3AC Entry into Processive Run—Our single molecule motility analysis (30) revealed that KIF3AC is more processive than KIF3AA or KIF3CC based on the run length data, implying that processivity is tuned in part by the intermolecular communication that occurs within the heterodimer. In addition, the results for MT association coupled with ADP release indicate a role for head-head communication because the behavior of KIF3AC is not equivalent to either KIF3AA or KIF3CC. To explore this hypothesis in greater detail, a direct comparison was made by measuring the kinetics of ADP release based on mantATP binding (Fig. 4). KIF3AC, KIF3AA, KIF3CC, and mixtures of KIF3AA + KIF3CC at 5 μM KIF3 site concentration were rapidly mixed with 30 μM MTs + 100 μM mantATP (syringe concentrations). The final concentrations were 2.5 μM KIF3 sites, 15 μM MTs, and 50 μM mantATP. The mixtures corresponded to 75% KIF3AA + 25% KIF3CC, 50% KIF3AA + 50% KIF3CC, and 25% KIF3AA + 75% KIF3CC with the final motor concentration at 2.5 μM after mixing (Fig. 4).

Note that for the KIF3AA + KIF3CC mixture experiments, KIF3AA MT collision is independent of KIF3CC MT collision. The data reported in Fig. 4*C* revealed that 100% KIF3AA resulted in the fastest rate of ADP release at 68 s^{-1}, consistent

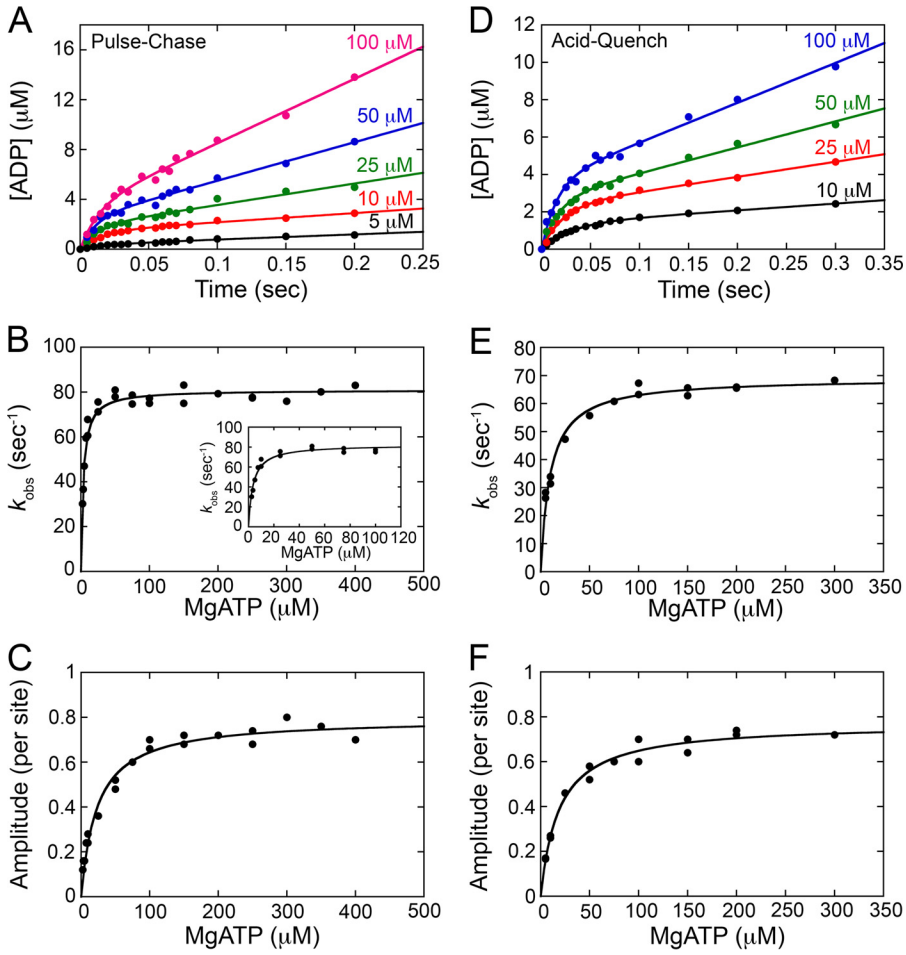

FIGURE 2. **Kinetics of ATP binding and ATP hydrolysis.** *A–C*, pulse-chase kinetics of ATP binding. The MT·KIF3AC complex was rapidly mixed in the chemical quench-flow instrument with increasing concentrations of MgATP plus trace [α-^{32}P]ATP and 300 mM KCl (syringe concentrations), followed by a chase with 30 mM unlabeled MgATP plus 150 mM KCl (syringe concentrations). The final concentrations were 2.5 or 5 μM KIF3AC, 20 μM MTs, 0–400 μM [α-^{32}P]ATP, and 150 mM KCl. *A*, representative transients display an initial exponential phase of [α-^{32}P]ADP·P_i formation corresponding to the first ATP turnover followed by a linear phase of product formation representing subsequent ATP turnovers. Equation 2 was fit to each transient. *B*, the observed rates of the initial exponential phase for individual transients were plotted as a function of MgATP concentration, and Equation 3 fit to the data provided $K_3 = 0.3 \pm 0.03$ μM^{-1}, $k'_{+3} = 81 \pm 1.0$ s^{-1}, and $K_{d,ATP} = 3.3$ μM. *C*, the amplitude of each exponential phase was normalized to the concentration of active sites and plotted as a function of MgATP concentration. The hyperbolic fit to the data provided the maximum $A_0 = 0.80 \pm 0.02$ μM ADP·P_i per μM site concentration and $K_{d,ATP} = 23.4 \pm 2.5$ μM. *D–F*, kinetics of ATP hydrolysis by acid-quench. The MT·KIF3AC complex was rapidly mixed with increasing concentrations of MgATP plus trace [α-^{32}P]ATP and 300 mM KCl. The final concentrations were 5 μM KIF3AC/15 μM MTs or 5 μM KIF3AC/20 μM MTs, 0–300 μM [α-^{32}P]ATP, and 150 mM KCl. *D*, representative transients show an initial burst phase followed by a linear phase of product formation representing subsequent ATP turnovers. Each transient was fit to Equation 2. *E*, the observed rates of the initial exponential phase for individual transients were plotted as a function of MgATP concentration, and the hyperbolic fit to the data provided $k_{+4} = 69.1 \pm 1.2$ s^{-1} and $K_{d,ATP} = 9.7 \pm 0.9$ μM. *F*, the amplitude of each burst phase was normalized to the concentration of active sites and plotted as a function of MgATP concentration. The hyperbolic fit to the data provided the maximum $A_0 = 0.77 \pm 0.02$ μM ADP·P_i per μM site concentration and $K_{d,ATP} = 18.8 \pm 1.9$ μM. The data shown in *B*, *C*, *E*, and *F* are from multiple experiments.

with the results in Fig. 3 at 15 μM MTs. Furthermore, each mixture of KIF3AA + KIF3CC resulted in an initial fast phase more similar to the rate for KIF3AA than KIF3AC at 36 s^{-1} and a slow phase of 4–5 s^{-1}. In fact, the 50% KIF3AA + 50% KIF3CC mixture resulted in a rate for ADP release at 62 s^{-1} for the initial fast phase attributed to KIF3AA and a second slow phase at 4.8 s^{-1} attributed to KIF3CC. Therefore, these results suggest that the kinetics for KIF3AC were not the sum of the kinetics of the independent KIF3A and KIF3C motor heads.

If one looks directly at the transients in Fig. 4 (*A* and *B*), there are differences in the amplitude associated with the initial fast and slow phases. For KIF3AA, almost all the amplitude is associated with the initial fast phase, indicating that ADP release from the first head was not well separated from ADP release from the second head. In contrast, for KIF3AC, the amplitude is split between the two phases, implying that the initial fast phase represents KIF3A and the slow phase represents KIF3C. The transients from the mixtures do show an initial fast phase that is similar to KIF3AA, but there is a progressive decrease in the total amplitude as the percentage of KIF3CC increases. Previous experiments for Fig. 3*D* showed that for KIF3CC, the slow rate of ADP release required a 1-s time domain for the stopped-flow experiment. Therefore, we attribute the decrease in amplitude for the mixtures and KIF3CC to be due to the shorter 0.5-s time domain of this experiment where the full amplitude cannot be observed. Importantly, the mixture of 50% KIF3AA plus 50% KIF3CC did not recapitulate the kinetics of 100% KIF3AC either in direct comparison of the transients or in comparison of the rates of ADP release (Fig. 4*C*).

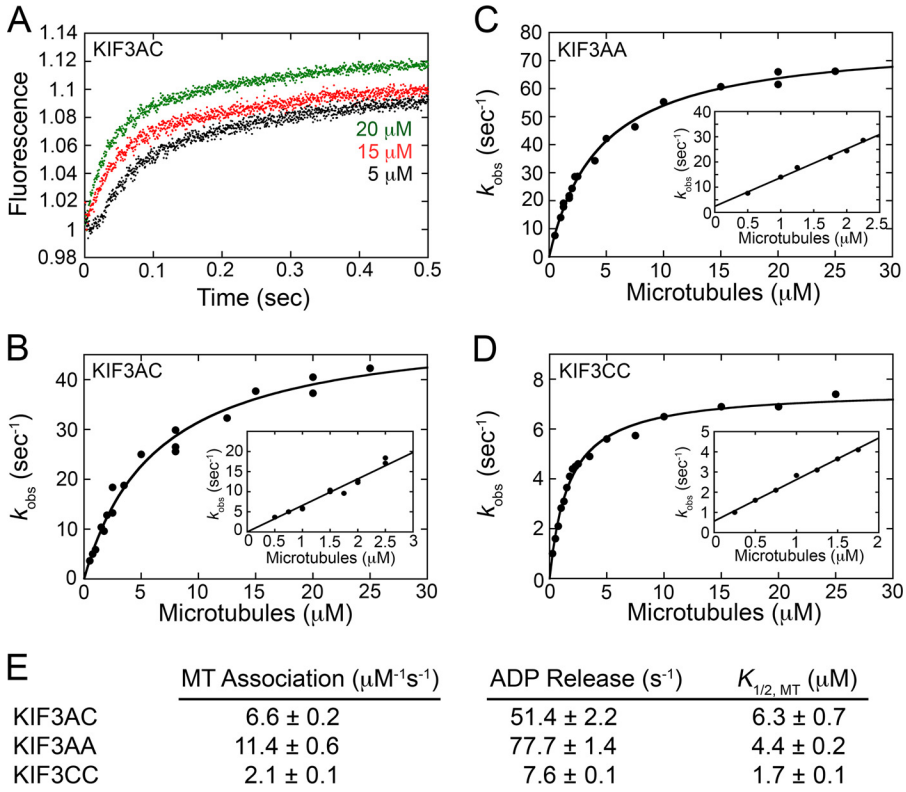

E

	MT Association ($\mu M^{-1}s^{-1}$)	ADP Release (s^{-1})	$K_{1/2,\,MT}$ (μM)
KIF3AC	6.6 ± 0.2	51.4 ± 2.2	6.3 ± 0.7
KIF3AA	11.4 ± 0.6	77.7 ± 1.4	4.4 ± 0.2
KIF3CC	2.1 ± 0.1	7.6 ± 0.1	1.7 ± 0.1

FIGURE 3. **ADP release upon MT collision for KIF3AC, KIF3AA and KIF3CC.** KIF3 was rapidly mixed in the stopped-flow instrument with varying concentrations of MTs plus mantATP. The final concentrations were 0.25 or 0.5 μM KIF3 sites/25 μM mantATP for 0.25–2.25 μM MTs or 2.5 μM KIF3 sites and 50 μM mantATP for 2.5–25 μM MTs. *A*, representative transients show a biphasic increase in mantATP fluorescence as a function of time. *B*, the observed rates of the initial exponential phase for each transient were plotted as a function of MT concentration, and the hyperbolic fit to the data provided the maximum rate constant of ADP release and the $K_{1/2,MT}$. *Inset*, at low MT concentrations, the data provided the second order rate constant for KIF3AC MT association. *C* and *D*, the kinetics of MT association followed by ADP release for KIF3AA (*C*) and KIF3CC (*D*). *E*, the constants for KIF3AC, KIF3AA, and KIF3CC.

If the experimental transient for 50% KIF3AA + 50% KIF3CC accurately represents the contribution from each motor head independently colliding with the MT, then a similar transient can be generated computationally using the data from the transients of 100% KIF3AA and 100% KIF3CC. Each transient represents 1,000 data points, and at each time point for the mixtures, it is the sum of the contribution from KIF3A plus KIF3C. Fig. 4*B* shows both the computationally generated transient for 50% KIF3AA + 50% KIF3CC (*gold*) relative to the experimental transient in *green*. Note that they superimpose on each other. Moreover, both the experimental and the computationally derived transients do not recapitulate the transient for KIF3AC (*red*).

This analysis supports our conclusion that MT collision by KIF3AA and KIF3CC in the mixture experiments represents independent events, and intermolecular communication between KIF3A and KIF3C can only occur within the heterodimeric KIF3AC. Furthermore, the results from Figs. 3 and 4 also reinforce the hypothesis that although either KIF3A or KIF3C can initiate the processive run, the influence of KIF3A on KIF3C and KIF3C on KIF3A is due to the intermolecular communication.

Discussion

The stepping model proposed in Fig. 5 illustrates the sequence of events by which a processive kinesin couples ATP turnover to each step along the MT. The cycle begins as one motor head of the dimer collides with the MT followed by ADP release (E0–E1). The asymmetry in the dimer is now established by which ATP turnover on one head is maintained out of phase with ATP turnover on the partner head. At E1, ATP binding at the leading head generates a series of structural transitions including neck linker docking onto the catalytic core and movement of the trailing ADP head forward to its next MT binding site, 16 nm ahead toward the MT plus end (E1–E4). ADP is subsequently released, which tightens the affinity of the leading head for the MT, thereby generating strain because the neck linkers are now in opposite orientations, and both heads are tightly bound to the MT (E4–E5). ATP hydrolysis is triggered on the trailing head followed by phosphate release coupled with detachment of the trailing head from the MT (E6–E7). This model proposes that ATP binding at the leading head of the E5 intermediate is inhibited because of the backward orientation of its neck linker and the intermolecular tension generated by the helix α7 coiled-coil (30, 34–38). The second step begins as the partner head binds ATP at E7.

For the homodimeric processive kinesins, the two motor domains in solution each have ADP tightly bound, and the asymmetry in the ATPase cycle is not established until MT collision. Therefore, a key question for heterodimeric KIF3AC is whether there is an intrinsic asymmetry in the heterodimer when in solution that favors KIF3A or KIF3C to initiate the processive run.

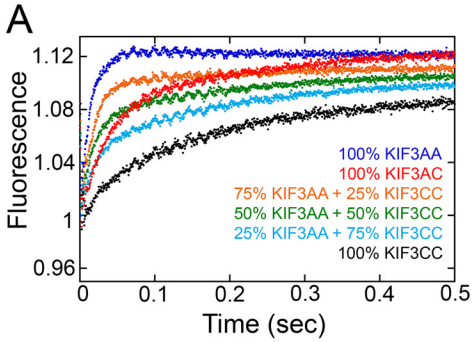

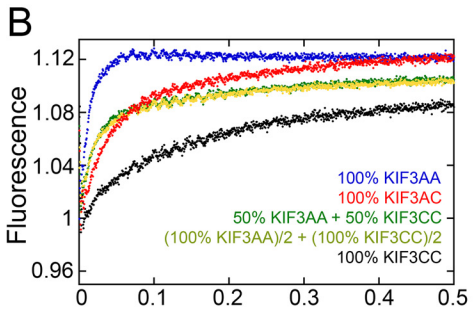

C

	ADP Release (s^{-1})
100% KIF3AC	35.9 ± 1.3
100% KIF3AA	67.7 ± 0.8
75% KIF3AA + 25% KIF3CC	64.2 ± 1.3
50% KIF3AA + 50% KIF3CC	62.0 ± 1.8
25% KIF3AA + 75% KIF3CC	60.1 ± 2.9
100% KIF3CC	10.2 ± 0.2

FIGURE 4. **ADP release upon MT collision for KIF3AC, KIF3AA, KIF3CC, and KIF3AA + KIF3CC.** 5 μM KIF3AC, KIF3AA, KIF3CC, or a mixture of KIF3AA plus KIF3CC at total 5 μM site concentration was rapidly mixed in the stopped-flow instrument with 30 μM MTs plus 100 μM mantATP (syringe concentrations). The mixture contains either 75% KIF3AA + 25% KIF3CC (3.75 μM KIF3AA and 1.25 μM KIF3CC), 50% KIF3AA + 50% KIF3CC (2.5 μM KIF3AA and 2.5 μM KIF3CC), or 25% KIF3AA + 75% KIF3CC (1.25 μM KIF3AA and 3.75 μM KIF3CC). The final concentrations were 2.5 μM KIF3 site concentration, 15 μM MTs, and 50 μM mantATP. *A*, individual transients show a biphasic increase in mantATP fluorescence as a function of time. Each transient was fit to a double exponential function, providing the observed rates of the initial exponential phase and reported in *C*. *B*, the experimental transients are shown as in *A*. The transient identified in *yellow* was determined computationally as described under "Experimental Procedures."

Entry into the Processive Run—The results presented indicate that either KIF3A or KIF3C can begin the processive run. The results in Fig. 3 show convincingly that the second order rate constant for MT association for KIF3AC is intermediate between those for KIF3AA and KIF3CC. Consistent with the kinetics for MT association, ADP release for KIF3AC following MT collision was also intermediate between the rate of ADP release for KIF3AA and KIF3CC. In fact, the ADP release kinetics suggest that there may be an equal probability of whether KIF3A or KIF3C initiates the processive run. Note that the rate of ADP release for KIF3AC at 51 s^{-1} is intermediate between the rates for KIF3AA at 78 s^{-1} and KIF3CC at 7.6 s^{-1}.

However, at first glance the pulse-chase and acid quench kinetics for ATP binding and ATP hydrolysis appear to suggest that it is not so simple where the rates at each step are the averages of KIF3AA and KIF3CC. The results from Fig. 2 show that for KIF3AC the ATP-promoted isomerization at 81 s^{-1} to form the intermediate poised for ATP hydrolysis is a fast step

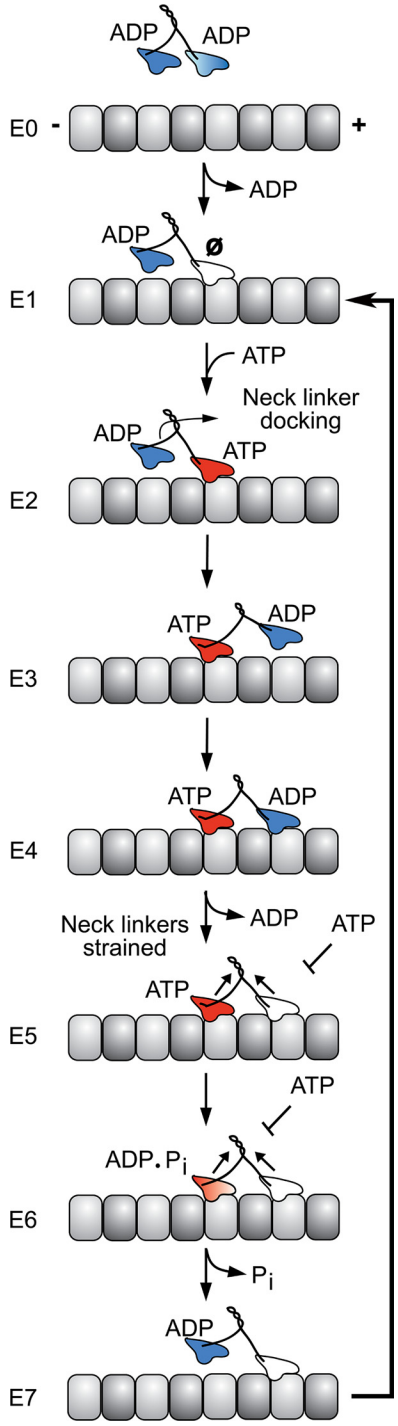

FIGURE 5. **KIF3AC Stepping model.** KIF3AC in solution and detached from the microtubule holds ADP tightly bound at each head (E0). The processive run begins upon MT collision by either the KIF3A or KIF3C head, followed by ADP release (E0 and E1). The leading head is nucleotide-free with the trailing head detached from the MT and ADP tightly bound. ATP binding at the leading head triggers a series of structural transitions including neck linker docking that promotes the trailing head to move forward to its next MT binding site (E2–E4). ADP is released upon MT collision, resulting in the E5 two-head-bound state. Strain develops between the two heads and inhibits its ATP binding to the nucleotide-free leading head (E5). ATP hydrolysis on the trailing head followed by phosphate (P_i) release relieves the interhead tension (E5–E7). The trailing head with ADP tightly bound has a weak affinity for the MT and thereby detaches (E7). The leading head can now bind ATP, which initiates the next step coupled to ATP turnover without detachment from the MT.

followed by ATP hydrolysis at 69 s^{-1}. Both of these rate constants are very fast. Furthermore, the maximum amplitude at ~0.8 per active site in each experiment suggests that both KIF3A and KIF3C were able to bind and hydrolyze ATP rapidly. If these rate constants only represented the contribution by KIF3A with exceedingly slow ATP binding and hydrolysis by KIF3C, then the amplitude expected would have been ~0.5 per site representing only the KIF3A head. Note too that the KIF3CC second order rate constant for mantATP binding (Fig. 1) at 0.68 $\mu M^{-1} s^{-1}$ predicts an ATP binding rate at 100 μM ATP of ~64 s^{-1}. Therefore, these data indicate that the kinetics observed for KIF3AC are consistent with the hypothesis that either KIF3A or KIF3C can initiate the processive run.

Impact of KIF3A on KIF3C and KIF3C on KIF3A—If the KIF3AC kinetics of MT collision and ADP release were simply the average of both heads as suggested for KIF3AB (31), then the kinetics for these steps should be consistent with the kinetics of a 1:1 mixture of homodimeric KIF3AA + KIF3CC equivalent in concentration to KIF3AC. The data in Fig. 4 clearly show that we were unable to generate a KIF3AC-like transient by using mixtures of KIF3AA + KIF3CC. Although the mixture of 25% KIF3AA + 75% KIF3CC (Fig. 4*A*, *blue transient*) was similar to the initial part of the KIF3AC transient (*red*), it failed to achieve the full amplitude of the initial exponential phase or a second exponential phase similar to that of KIF3AC. Comparison of the KIF3AC transient to the transient from 50% KIF3AA + 50% KIF3CC (*green*) also shows that the mixture of the homodimers did not recapitulate the kinetics of KIF3AC. Therefore, these results show that although the processive run may begin with either KIF3A or KIF3C motor domain collision with the MT, the kinetics observed are an emergent property caused by intermolecular communication within the heterodimer rather than the average of the intrinsic behavior of each motor head.

Key Questions Ahead—Although these initial studies have provided a much better understanding of entry into the processive run, there is much that is still unknown. One key question is whether once in a processive run, the KIF3A and KIF3C heads retain their intrinsic mechanochemistry or rather because of the heterodimerization, do KIF3A and KIF3C become similar with a unique emergent mechanochemistry because of intermolecular communication. The results presented here, the single molecule velocity rates, and the steady-state ATPase k_{cat} parameters suggest that intermolecular interactions within the heterodimer result in each motor head regulating the other (Table 1 and Ref. 30). Thus, we may discover that the influence of KIF3A on KIF3C and KIF3C on KIF3A may yield a heterodimer that behaves not so differently from a homodimer after all.

Author Contributions—P. Z., I. R., and S. P. G. designed the research; P. Z. performed the research; and P. Z., I. R., and S. P. G. analyzed the data and wrote the manuscript.

Acknowledgments—We thank Dr. Stephanie Guzik-Lendrum, Clay Albracht, Brandon Bensel, Sean Quinn, and Becky Phillips for thoughtful discussions and input on these experiments and analyses.

References

1. Hirokawa, N., Niwa, S., and Tanaka, Y. (2010) Molecular motors in neurons: transport mechanisms and roles in brain function, development, and disease. *Neuron* **68,** 610–638
2. Verhey, K. J., Kaul, N., and Soppina, V. (2011) Kinesin assembly and movement in cells. *Annu. Rev. Biophys.* **40,** 267–288
3. Scholey, J. M. (2013) Kinesin-2: a family of heterotrimeric and homodimeric motors with diverse intracellular transport functions. *Annu. Rev. Cell Dev. Biol.* **29,** 443–469
4. Aizawa, H., Sekine, Y., Takemura, R., Zhang, Z., Nangaku, M., and Hirokawa, N. (1992) Kinesin family in murine central nervous system. *J. Cell Biol.* **119,** 1287–1296
5. Kondo, S., Sato-Yoshitake, R., Noda, Y., Aizawa, H., Nakata, T., Matsuura, Y., and Hirokawa, N. (1994) KIF3A is a new microtubule-based anterograde motor in the nerve axon. *J. Cell Biol.* **125,** 1095–1107
6. Yamazaki, H., Nakata, T., Okada, Y., and Hirokawa, N. (1995) KIF3A/B: A heterodimeric kinesin superfamily protein that works as a microtubule plus end-directed motors for membrane organelle transport. *J. Cell Biol.* **130,** 1387–1399
7. Sardella, M., Navone, F., Rocchi, M., Rubartelli, A., Viggiano, L., Vignali, G., Consalez, G. G., Sitia, R., and Cabibbo, A. (1998) KIF3C, a novel member of the kinesin superfamily: sequence, expression, and mapping to human chromosome 2 at 2p23. *Genomics* **47,** 405–408
8. Muresan, V., Abramson, T., Lyass, A., Winter, D., Porro, E., Hong, F., Chamberlin, N. L., and Schnapp, B. J. (1998) KIF3C and KIF3A form a novel neuronal heteromeric kinesin that associates with membrane vesicles. *Mol. Biol. Cell* **9,** 637–652
9. Nonaka, S., Tanaka, Y., Okada, Y., Takeda, S., Harada, A., Kanai, Y., Kido, M., and Hirokawa, N. (1998) Randomization of left-right asymmetry due to loss of nodal cilia generating leftward flow of extraembryonic fluid in mice lacking KIF3B motor protein. *Cell* **95,** 829–837
10. Yang, Z., and Goldstein, L. S. (1998) Characterization of the KIF3C neural kinesin-like motor from mouse. *Mol. Biol. Cell* **9,** 249–261
11. Takeda, S., Yonekawa, Y., Tanaka, Y., Okada, Y., Nonaka, S., and Hirokawa, N. (1999) Left-right asymmetry and kinesin superfamily protein KIF3A: new insights in determination of laterality and mesoderm induction by kif3A$^{-/-}$ mice analysis. *J. Cell Biol.* **145,** 825–836
12. Marszalek, J. R., Ruiz-Lozano, P., Roberts, E., Chien, K. R., and Goldstein, L. S. (1999) Situs inversus and embryonic ciliary morphogenesis defects in mouse mutants lacking the KIF3A subunit of kinesin-II. *Proc. Natl. Acad. Sci. U.S.A.* **96,** 5043–5048
13. Marszalek, J. R., Liu, X., Roberts, E. A., Chui, D., Marth, J. D., Williams, D. S., and Goldstein, L. S. (2000) Genetic evidence for selective transport of opsin and arrestin by kinesin-II in mammalian photoreceptors. *Cell* **102,** 175–187
14. Takeda, S., Yamazaki, H., Seog, D. H., Kanai, Y., Terada, S., and Hirokawa, N. (2000) Kinesin superfamily protein 3 (KIF3) motor transports fodrin-associating vesicles important for neurite building. *J. Cell Biol.* **148,** 1255–1265
15. Setou, M., Nakagawa, T., Seog, D. H., and Hirokawa, N. (2000) Kinesin superfamily motor protein KIF17 and mLin-10 in NMDA receptor-containing vesicle transport. *Science* **288,** 1796–1802
16. Navone, F., Consalez, G. G., Sardella, M., Caspani, E., Pozzoli, O., Frassoni, C., Morlacchi, E., Sitia, R., Sprocati, T., and Cabibbo, A. (2001) Expression of KIF3C kinesin during neural development and in vitro neuronal differentiation. *J. Neurochem.* **77,** 741–753
17. Yang, Z., Roberts, E. A., and Goldstein, L. S. (2001) Functional analysis of mouse kinesin motor Kif3C. *Mol. Cell. Biol.* **21,** 5306–5311
18. Cole, D. G., Chinn, S. W., Wedaman, K. P., Hall, K., Vuong, T., and Scholey, J. M. (1993) Novel heterotrimeric kinesin-related protein purified from sea urchin eggs. *Nature* **366,** 268–270
19. Yamazaki, H., Nakata, T., Okada, Y., and Hirokawa, N. (1996) Cloning and characterization of KAP3: a novel kinesin superfamily-associated protein of KIF3A/3B. *Proc. Natl. Acad. Sci. U.S.A.* **93,** 8443–8448
20. Wedaman, K. P., Meyer, D. W., Rashid, D. J., Cole, D. G., and Scholey, J. M. (1996) Sequence and submolecular localization of the 115-kD accessory subunit of the heterotrimeric kinesin-II (KRP85/95) complex. *J. Cell Biol.*

132, 371–380
21. Shimizu, K., Shirataki, H., Honda, T., Minami, S., and Takai, Y. (1998) Complex formation of SMAP/KAP3, a KIF3A/B ATPase motor-associated protein, with a human chromosome-associated polypeptide. *J. Biol. Chem.* **273,** 6591–6594
22. Teng, J., Rai, T., Tanaka, Y., Takei, Y., Nakata, T., Hirasawa, M., Kulkarni, A. B., and Hirokawa, N. (2005) The KIF3 motor transports N-cadherin and organizes the developing neuroepithelium. *Nat. Cell Biol.* **7,** 474–482
23. Davidovic, L., Jaglin, X. H., Lepagnol-Bestel, A. M., Tremblay, S., Simonneau, M., Bardoni, B., and Khandjian, E. W. (2007) The fragile X mental retardation protein is a molecular adaptor between the neurospecific KIF3C kinesin and dendritic RNA granules. *Hum. Mol. Genet.* **16,** 3047–3058
24. Nekrasova, O. E., Amargo, E. V., Smith, W. O., Chen, J., Kreitzer, G. E., and Green, K. J. (2011) Desmosomal cadherins utilize distinct kinesins for assembly into desmosomes. *J. Cell Biol.* **195,** 1185–1203
25. Guo, H. L., Zhang, C., Liu, Q., Li, Q., Lian, G., Wu, D., Li, X., Zhang, W., Shen, Y., Ye, Z., Lin, S. Y., and Lin, S. C. (2012) The Axin/TNKS complex interacts with KIF3A and is required for insulin-stimulated GLUT4 translocation. *Cell Res.* **22,** 1246–1257
26. Carpenter, B. S., Barry, R. L., Verhey, K. J., and Allen, B. L. (2015) The heterotrimeric kinesin-2 complex interacts with and regulates GLI protein function. *J. Cell Sci.* **128,** 1034–1050
27. Prevo, B., Mangeol, P., Oswald, F., Scholey, J. M., and Peterman, E. J. (2015) Functional differentiation of cooperating kinesin-2 motors orchestrates cargo import and transport in *C. elegans* cilia. *Nat. Cell Biol.* **17,** 1536–1545
28. Huang, C. F., and Banker, G. (2012) The translocation selectivity of the kinesins that mediate neuronal organelle transport. *Traffic* **13,** 549–564
29. Rank, K. C., and Rayment, I. (2013) Functional asymmetry in kinesin and dynein dimers. *Biol. Cell* **105,** 1–13
30. Guzik-Lendrum, S., Rank, K. C., Bensel, B. M., Taylor, K. C., Rayment, I., and Gilbert, S. P. (2015) Kinesin-2 KIF3AC and KIF3AB can drive long-range transport along microtubules. *Biophys. J.* **109,** 1472–1482
31. Andreasson, J. O., Shastry, S., Hancock, W. O., and Block, S. M. (2015) The mechanochemical cycle of mammalian kinesin-2 KIF3A/B under load. *Curr. Biol.* **25,** 1166–1175
32. Albracht, C. D., Rank, K. C., Obrzut, S., Rayment, I., and Gilbert, S. P. (2014) Kinesin-2 KIF3AB exhibits novel ATPase characteristics. *J. Biol. Chem.* **289,** 27836–27848
33. Zhang, P., Dai, W., Hahn, J., and Gilbert, S. P. (2015) *Drosophila* Ncd reveals an evolutionarily conserved powerstroke mechanism for homodimeric and heterodimeric kinesin-14s. *Proc. Natl. Acad. Sci. U.S.A.* **112,** 6359–6364
34. Clancy, B. E., Behnke-Parks, W. M., Andreasson, J. O., Rosenfeld, S. S., and Block, S. M. (2011) A universal pathway for kinesin stepping. *Nat. Struct. Mol. Biol.* **18,** 1020–1027
35. Hyeon, C., and Onuchic, J. N. (2007) Internal strain regulates the nucleotide binding site of the kinesin leading head. *Proc. Natl. Acad. Sci. U.S.A.* **104,** 2175–2180
36. Hyeon, C., and Onuchic, J. N. (2007) Mechanical control of the directional stepping dynamics of the kinesin motor. *Proc. Natl. Acad. Sci. U.S.A.* **104,** 17382–17387
37. Bornschlögl, T., Woehlke, G., and Rief, M. (2009) Single molecule mechanics of the kinesin neck. *Proc. Natl. Acad. Sci. U.S.A.* **106,** 6992–6997
38. Dogan, M. Y., Can, S., Cleary, F. B., Purde, V., and Yildiz, A. (2015) Kinesin's front head is gated by the backward orientation of its neck linker. *Cell Rep.* **10,** 1967–1973